



Simultaneous design of non-Newtonian lubricant and surface texture using surrogate-based multiobjective optimization

Yong Hoon Lee¹ · Jonathon K. Schuh² · Randy H. Ewoldt³ · James T. Allison⁴

Received: 7 August 2018 / Revised: 12 November 2018 / Accepted: 6 January 2019 / Published online: 22 January 2019
© Springer-Verlag GmbH Germany, part of Springer Nature 2019

Abstract

Surface textures decrease friction in lubricated sliding with Newtonian fluids. Viscoelastic non-Newtonian lubricants can enhance frictional performance, but the optimal rheological material properties and their coupling to the texture design are non-obvious. In this study, we present a simultaneous design of both surface texture shape and non-Newtonian properties, which can be achieved by fluid additives that introduce viscoelasticity, shear thinning, and normal stress differences. Two models with different fidelity and computational cost are used to model laminar non-Newtonian fluid flow between a rotating flat plate and a textured disk. At lower fidelity, we use the Criminale-Ericksen-Filbey (CEF) constitutive model and a thin-film approximation for conservation of momentum (Reynolds equation). At higher fidelity, we use a fully nonlinear constitutive model typically applicable to polymer solutions (multimode Giesekus model) and the full 3-D momentum equations. Fluid additive design is parameterized by two relaxation modes each having a timescale, added viscosity, and a nonlinear anisotropic drag parameter. To manage the computational complexity and constraints between design variables, we use our previously developed multiobjective adaptive surrogate modeling-based optimization (MO-ASMO) method. A new data-driven extension of MO-ASMO is introduced that constructs general boundaries to prevent attempts to evaluate designs that would lead to simulation failure. We demonstrate the efficiency of our MO-ASMO method and provide insights into co-designing the lubricant and textured surface. The Pareto-optimal solutions include fluid designs with both high and low viscoelastic additive loading. We rationalize this trade-off and discuss how the optimal design targets can be physically realized.

Keywords Simultaneous co-design · Non-Newtonian lubricant · Nonlinear viscoelasticity · Surrogate-based optimization

1 Introduction

Surface textures decrease friction in lubricated sliding contact with Newtonian fluids (Wakuda et al. 2003; Etsion 2004; Johnston et al. 2015). In hydrodynamic lubrication applications, surface texturing helps generate hydrodynamic

pressure to support loads (Hamilton et al. 1966; Lee et al. 2017b; Schuh et al. 2017), provide reservoirs for lubricant (Wakuda et al. 2003; Hamilton et al. 1966; Pettersson and Jacobson 2003), decrease shear stress (Wakuda et al. 2003; Etsion 2004; Johnston et al. 2015; Hamilton et al. 1966; Lee et al. 2017b; Schuh et al. 2017; Pettersson and Jacobson 2003; Gropper et al. 2016), and trap debris to help prevent surface wear and damage (Suh et al. 1994; Varenberg et al. 2002). We previously have shown that this friction reduction can be enhanced further using more general surface topographies (Lee et al. 2017b); this recent work in freeform texture design was motivated by earlier studies that showed favorable surface shapes can enhance frictional characteristics (Yu et al. 2010). For the study presented in Lee et al. (2017b), we developed surface parameterization techniques for generating an arbitrary texture profile subject to local slope (manufacturability) constraints. We modeled the flow of an incompressible Newtonian fluid over the textured surfaces using the Reynolds equation (Schuh et al.

Responsible Editor: Felipe A. C. Viana

This work was presented in part at the AIAA SciTech Forum 2018, Kissimmee, FL, January 8–12, 2018. Y. H. Lee and J. K. Schuh contributed equally to this work.

Electronic supplementary material The online version of this article (<https://doi.org/10.1007/s00158-019-02201-1>) contains supplementary material, which is available to authorized users.

✉ Yong Hoon Lee
ylee196@illinois.edu

Extended author information available on the last page of the article.

Table 1 Fluid models used for design in this study and corresponding solver governing equations

Case no.	Fluid model	Governing equation	Dimension
1	CEF model	Reynolds equation	2-D (r, θ)
2	Giesekus model	Cauchy momentum equation	3-D (r, θ, z)
0	Newtonian fluid	Cauchy momentum equation	3-D (r, θ, z)

2017; Reynolds 1886) and used this model to determine the optimal texture profile for minimizing frictional loss (shear stress) and maximizing load capacity (normal force).

We have also studied friction reduction experimentally with surface textures and viscoelastic non-Newtonian lubricants (Schuh 2015a, b). Viscoelastic non-Newtonian lubricants can decrease shear stress due to shear thinning (Batra and Mohan 1978; Hirani et al. 2008) and increase the load capacity due to normal stress differences (Xiaodi et al. 2009). Combining these additional fluid properties with surface texturing results in greater friction reduction than when either strategy is used independently (Schuh 2015a, b). However, optimization of these viscoelastic properties, or the combined optimization of both fluid and surface texture, has not been considered previously.

Based on these observations, we extend our design study to include viscoelastic non-Newtonian fluid effects in friction reduction. A key challenge is the paradigm of how to “design” the non-Newtonian fluid behavior. There is no single mathematical model to describe all possible non-Newtonian fluids in the nonlinear viscoelastic regime (Ewoldt 2014), although universal equations apply in some limited circumstances, such as very small deformations with linear viscoelastic design (Corman et al. 2016). Nonlinear viscoelastic design is of interest here, and we consider two different constitutive models with different fidelities, though both are parameterized by the same fluid design parameters. Selecting the fluid design description is also nontrivial. Here, we focus on continuum-level descriptions that can be applicable to a range of possible fluid additives, rather than material-specific parameters such as polymer

molecular weight or colloid size, which would depend on the specific material embodiment to achieve the desired rheology. Our results here serve as targets that can be achieved by a wide range of material classes (resulting in a rheological inverse problem (Nelson and Ewoldt 2017)); however, we expect polymer solutions to be the most likely formulation.

We include viscoelastic effects through two different models: the Criminale-Ericksen-Filbey (CEF) model and a multimode Giesekus model. The flow fields with both models are three dimensional; however, the CEF model is less computationally expensive because it can be used in the thin-film limit (Ashmore et al. 2008) to derive a modified Reynolds equation (which we have done, see the Supplementary Materials and Schuh 2018) that includes viscoelastic effects, whereas the multimode Giesekus model is used with the full 3-D Cauchy momentum equations. Combinations of the fluid models and governing equations are given in Table 1, and are discussed in more detail in Sections 2.1 and 3.1. We compare the results from the viscoelastic models to the Newtonian fluid reference case for the following reasons: first, the simplest models for including viscoelasticity are based on perturbations around the Newtonian fluid model (ordered fluid expansion (Bird et al. 1987)), and second, we are interested in comparing the system performance with viscoelasticity to the conventional Newtonian lubricants.

Figure 1 illustrates the design problem presented. We have adapted our previous design optimization strategy (Lee et al. 2017b; Schuh et al. 2017) to design both surface texture topography and non-Newtonian viscometric

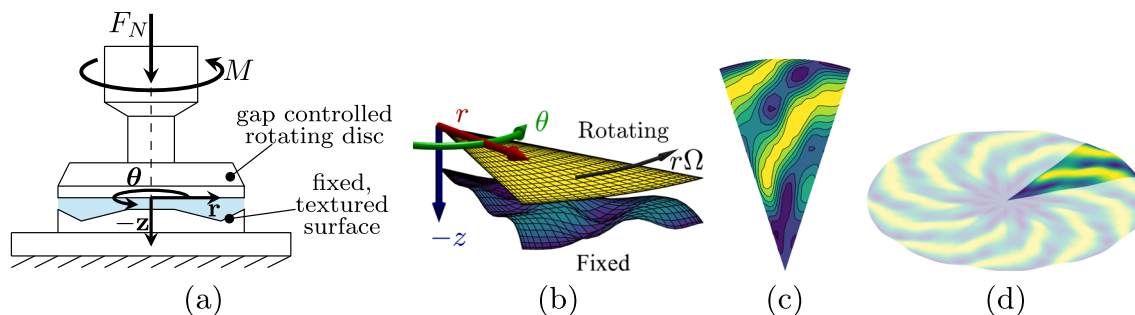


Fig. 1 A lubricated periodic surface texture design problem in a rotational tribo-rheometer setting. **a** Schematic diagram; **b** simulated periodic sector; **c** sector design; **d** full disc design

functions. Figure 1a shows the setup used previously in experiments (Schuh 2015a); the fluid is confined between a flat plate that rotates at a constant angular velocity and a stationary textured surface. A sector shown in Fig. 1b and c is an example design of the surface texture height profiles as a function of r and θ . Figure 1d shows an example of a fully textured disc using ten periodic sectors.

As we extend our study to include nonlinear viscoelastic models, and move from 2-D to 3-D, the computational cost associated with the design problem increases significantly. In our previous study, where we modeled the fluid flow with the (Newtonian) Reynolds equation, the computational cost of the optimization was reduced by using a coarse design mesh that was mapped onto a finer analysis mesh (Lee et al. 2017b). The computational cost of the optimization can also be reduced by linearizing the Reynolds equation (with respect to the design variables) and iteratively solving using a sequential linear programming (SLP) strategy (Lin et al. 2018) or by adaptively constructing computationally efficient surrogate models of expensive simulation responses (Wang and Shan 2007). Here, we solve the full nonlinear optimization problem using surrogate modeling. We have developed a multiobjective adaptive surrogate modeling-based optimization (MO-ASMO) strategy (Lee et al. 2017a) that uses efficient sampling techniques to explore a constrained design space and search for Pareto-optimal solutions. This algorithm is developed specifically for problems with narrow or geometrically complex feasible design domains. We have imposed a local slope constraint on the gap height profile (manufacturability constraint) and have constrained the viscoelastic material functions using the analytical solution of the Giesekus model in steady simple shear flow to represent realizable materials using a limited number of fluid parameters. It is demonstrated that the MO-ASMO algorithm is beneficial by reducing the overall computational cost of the combined fluid and texture design optimization problem.

Our contributions in this study are summarized here.

- We demonstrate that simultaneous co-design of texture (structural shape) and rheology (material properties) achieves better frictional system performance than design employing only texture shape optimization (as done previously). Our design is uniquely achieved by parameterizing the target viscometric functions, such as viscosity and first normal stress difference.
- We propose two unique non-Newtonian fluid solvers specifically for design applications involving surface texture shape design. We first suggest modeling the viscoelastic behavior with the CEF model, and use this constitutive relationship to derive a modified form of the Reynolds equation (CEF-Reynolds equation), which includes leading order viscoelasticity and inertia, in cylindrical coordinates. The solution of the CEF-Reynolds equation is obtained in nearly the same time as the traditional Reynolds equation, but the solution also includes leading order viscoelastic and inertial effects that the Reynolds equation does not. The fidelity of the model can be improved by using the full 3-D Cauchy momentum equations in cylindrical coordinates, which we also use here, where the additional polymeric shear stress is included by a multimode Giesekus model. This representation also includes time-dependent fluid behavior (for example, relaxation) that is not included in the CEF-Reynolds equation. While this model increases design fidelity, it comes at the cost of a longer simulation time. Both of these models are discretized using the pseudospectral method, which has many advantages over other discretization techniques for simulation-based optimization, as explained in Section 3.1.3.
- The design representation allows for determining physically realizable material functions, independent of material formulation. The CEF model is material-independent, and the model parameters are the shear-rate dependent viscosity and normal stress differences, which can be parameterized in any arbitrary way. Achieving these independent material properties with real materials requires the use of material-specific constitutive models (such as the Giesekus model, which applies for polymer solutions, polymer melts, worm-like micelles, etc.) where the material properties are related through parameters that have physical meanings, such as polymer relaxation time.
- Finally, we show that actively updated bounds that encapsulate the infeasible region using the support vector domain description (SVDD) method makes possible the avoidance of design space regions that lead to numerical instabilities and simulation failure. SVDD accommodates very general boundaries, and this strategy improves overall computational efficiency.

This paper is organized as follows. Section 2 presents the two non-Newtonian fluid models and the design problem formulation. Section 3 introduces solution procedures for fluid flow and surrogate-based design optimization. Section 4 presents the results and discusses the impact of using different fluid models on the design problem results. Section 5 then summarizes the results and concludes with the main findings from this study.

2 Formulation

We use models of two different fidelities, but both are governed by conservation of mass, momentum, and a constitutive

equation for the fluid stress $\underline{\underline{\tau}}$. The different fidelities result from different simplifying assumptions of these governing equations. Conservation of mass (incompressible flow) and momentum are given by the following:

$$\nabla \cdot \underline{u} = 0 \quad (1a)$$

$$\rho \left(\frac{\partial \underline{u}}{\partial t} + [\underline{u} \cdot \nabla] \underline{u} \right) = -\nabla p + \nabla \cdot \underline{\underline{\tau}}, \quad (1b)$$

where \underline{u} is the velocity field, ρ is fluid density, p is the isotropic pressure, and $\underline{\underline{\tau}}$ is the material stress. Fluid design parameters will appear in the material stress through the constitutive model for $\underline{\underline{\tau}}$.

We model this scenario at two different fidelities: one used the full 3-D conservation of momentum for the flow field with a high-fidelity nonlinear viscoelastic constitutive equation for the stress tensor. The thin-film geometry and dynamic conditions motivate a lower fidelity model that neglects complexities in both the governing momentum equation and the constitutive model. For this, we use a non-Newtonian fluid model that captures the nonlinear rheological behavior but only weak viscoelasticity and simplify the governing equations based on thin-film (lubrication approximation) concepts that neglect certain spatial derivatives in (1b). The governing constitutive equations for $\underline{\underline{\tau}}$, which involve the *fluid* design parameters, are described in the following subsections.

2.1 Non-Newtonian fluid models

Non-Newtonian fluids show different rheological behavior than Newtonian fluids; the behaviors most often studied are shear thinning, viscoelasticity, generation of normal stresses in shear, and extensional thickening. These rheological behaviors can be described using different constitutive models. The two models we use are the CEF model and the multimode Giesekus model.

We select these two models because of their ability to predict shear thinning, normal stress generation, and viscoelasticity (more details given below). The higher fidelity Giesekus model is fully nonlinear and viscoelastic. It is derived in the context of polymeric systems (often used for polymer solutions and polymer melts) and is parameterized by $3k$ parameters, where k is the total number of relaxation modes. We limit ourselves here to $k = 2$ determined by the Bayesian information criterion (BIC), an approximation of the full Bayes factors (Schwarz 1978). Readers are referred to Appendix A.3 in Schuh (2018) for the detailed procedure used to determine the parameter k . The CEF model is lower fidelity, but is universally applicable to all non-Newtonian fluids in the limit of weak viscoelasticity. Thus, it can support a larger design space for achieving a given fluid behavior. The inputs to the CEF model are functions, which need to be parameterized;

here, we choose to parameterize the rheological material functions for the CEF model using the steady shear material behavior for the Giesekus model, which allows us to have the proper interrelations between the viscosity and normal stress differences. Thus, both models have the same fluid design parameters consisting of two relaxation modes each having a timescale, added viscosity, and a nonlinear anisotropic drag parameter: $(\lambda_k, \eta_k, \alpha_k)$.

2.1.1 Criminale-Ericksen-Filbey (CEF) model

The CEF model (Criminale et al. 1957; Bird et al. 1987) is a constitutive model for the stress tensor $\underline{\underline{\tau}}$ that contains terms for the shear-rate dependent viscosity and the first and second normal stress differences, and is given as follows:

$$\underline{\underline{\tau}} = \eta(\dot{\gamma}) \underline{\underline{\gamma}}_{(1)} - \frac{1}{2} \Psi_1(\dot{\gamma}) \underline{\underline{\gamma}}_{(2)} + \Psi_2(\dot{\gamma}) \left(\underline{\underline{\gamma}}_{(1)} \cdot \underline{\underline{\gamma}}_{(1)} \right), \quad (2)$$

where the upper convected time derivative (Oldroyd 1950) of the shear rate $\dot{\underline{\underline{\gamma}}}$ is defined as follows:

$$\dot{\underline{\underline{\gamma}}} = \underline{\underline{\gamma}}_{(1)} = \nabla \underline{u} + (\nabla \underline{u})^T, \quad \text{and} \quad (3a)$$

$$\underline{\underline{\gamma}}_{(n+1)} = \frac{\partial \underline{\underline{\gamma}}_{(n)}}{\partial t} + (\underline{u} \cdot \nabla) \underline{\underline{\gamma}}_{(n)} - \left((\nabla \underline{u})^T \cdot \underline{\underline{\gamma}}_{(n)} + \underline{\underline{\gamma}}_{(n)} \cdot (\nabla \underline{u}) \right). \quad (3b)$$

The model parameters are the functions $\eta(\cdot)$, $\Psi_1(\cdot)$, and $\Psi_2(\cdot)$, which are equivalent to the viscometric functions in simple shear. For general flow fields, these functions depend on the instantaneous shear-rate magnitude $\dot{\gamma}$ where $\dot{\gamma} = \sqrt{\frac{1}{2} \dot{\underline{\underline{\gamma}}} : \dot{\underline{\underline{\gamma}}}}$ (the operator ‘:’ denotes the inner product of tensors). The first term in (2) models a generalized Newtonian fluid, and the remaining terms model the behavior of elastic effects from normal stress differences.

In steady, simple shear flow, where $\underline{u} = \dot{\gamma} y \hat{i}$, the CEF model gives the shear viscosity η , and the first and second normal stress difference coefficients Ψ_1 and Ψ_2 as $\eta = \eta(\dot{\gamma})$, $\Psi_1 = \Psi_1(\dot{\gamma})$, $\Psi_2 = \Psi_2(\dot{\gamma})$, meaning that the inputs to the CEF model are the steady shear responses for a given fluid. It should be noted that for most polymeric systems, $\Psi_2(\dot{\gamma}) < 0$.

In small amplitude oscillatory shear, where $\underline{u} = \gamma_0 \omega \cos(\omega t) y \hat{i}$, γ_0 is the strain amplitude, and ω is the angular frequency, the CEF model gives the dynamic viscosity η' and the storage modulus G' as follows:

$$\eta' = \eta(\dot{\gamma} = 0) \quad (4a)$$

$$G' = \frac{1}{2} \Psi_1(\dot{\gamma} = 0) \omega^2 \quad (4b)$$

which is the same behavior as that predicted by the second-order fluid (SOF) model, which gives the first-order deviation from Newtonian fluid behavior, and is the same terminal regime (limit $\omega \rightarrow 0$) predicted by all fully nonlinear fluid models (including polymer systems) with a finite longest relaxation time.

The design inputs for this model are the rheological material functions $\eta(\dot{\gamma})$, $\Psi_1(\dot{\gamma})$, and $\Psi_2(\dot{\gamma})$. There are infinitely many ways of representing the material functions; here, we choose to use the steady shear response from fully nonlinear models, which reduces the fluid design representation to the design inputs λ_k , η_{pk} , and α_k , which are related to the steady-state behavior of $\eta(\dot{\gamma})$, $\Psi_1(\dot{\gamma})$, and $\Psi_2(\dot{\gamma})$ for a multimode Giesekus model (Bird et al. 1987) as follows:

$$\eta = \eta_s + \sum_{k=1}^{n_{mode}} \eta_{pk} \frac{(1 - f_k)^2}{1 + (1 - 2\alpha_k) f_k} \tag{5}$$

$$\Psi_1 = \sum_{k=1}^{n_{mode}} 2\eta_{pk} \lambda_k \frac{f_k (1 - \alpha_k f_k)}{(\lambda_k \dot{\gamma})^2 \alpha_k (1 - f_k)} \tag{6}$$

$$\Psi_2 = \sum_{k=1}^{n_{mode}} \eta_{pk} \lambda_k \left(\frac{-f_k}{(\lambda_k \dot{\gamma})^2} \right) \tag{7}$$

where,

$$f_k = \frac{1 - \chi_k}{1 + (1 - 2\alpha_k) \chi_k} \tag{8a}$$

$$\chi_k^2 = \frac{\sqrt{1 + 16\alpha_k (1 - \alpha_k) (\lambda_k \dot{\gamma})^2} - 1}{8\alpha_k (1 - \alpha_k) (\lambda_k \dot{\gamma})^2}. \tag{8b}$$

We use this model because of the predicted normal stress generation which is important in determining the thrust generation with polymer solutions. We limit the parameters $\eta_{pk} \in [0, \frac{5}{2}\eta_s]$, $\lambda_k \in [10^{-5}, 10^{-2}]$ (sec), and $\alpha_k \in [0.01, 0.5]$. The bounds on η_{pk} are determined by fitting the Huggins equation (Huggins 1942) to experimental data of zero shear viscosity as a function of polymer concentration, and noting the region where the Huggins equation is valid when compared to the experimental data. The bounds on λ_k are also determined from fitting the Giesekus model to experimental data for polymer solutions at varying concentrations of polyisobutylene (PIB) (Schuh 2018), which are also within the range of concentrations tested here. The mobility factor α_k is bounded between 0.01 and 0.5 to ensure realistic material properties (Atalık and Keunings 2004). When α_k is less than 0.01, large Weissenberg numbers $Wi = \lambda\dot{\gamma}$ cause numerical instability, and numerical computation tends to fail (Keunings 2000). The total number of fluid design variables is $3k$, where k is the number of relaxation modes in the parameterization.

2.1.2 Multimode Giesekus model

The CEF model only captures viscoelasticity in the limit of low frequency, close to steady state. To capture the higher order viscoelastic effects, we must use a higher fidelity model that captures the full range of the viscoelastic

response. Here, we choose a multimode Giesekus model to simulate our polymeric stresses (Bird et al. 1987), given as follows:

$$\lambda_k \left(\frac{\partial \underline{\tau}_{pk}}{\partial t} + (\underline{u} \cdot \nabla) \underline{\tau}_{pk} - [(\nabla \underline{u})^T \cdot \underline{\tau}_{pk} + \underline{\tau}_{pk} \cdot (\nabla \underline{u})] \right) + \underline{\tau}_{pk} + \frac{\lambda_k \alpha_k}{\eta_{pk}} (\underline{\tau}_{pk} \cdot \underline{\tau}_{pk}) = \eta_{pk} \dot{\underline{\gamma}}, \tag{9}$$

where λ_k is the relaxation time, η_{pk} is the polymeric viscosity, and α_k is the mobility factor of the k th mode which can be physically related to the anisotropic drag of a polymer when deformed by the flow. Note that the entire first term in parentheses on the left-hand side is an upper convected time derivative of the polymeric stress $\underline{\tau}_{pk}$. The contributions from each mode are assumed to be additive such that the total polymeric stress $\underline{\tau}_p$ is given as follows:

$$\underline{\tau}_p = \sum_{k=1}^{n_{mode}} \underline{\tau}_{pk}. \tag{10}$$

The steady shear viscosity and normal stress differences are the same as those given in (5)-(7). Here, the linear (small amplitude) viscoelastic behavior (Bird et al. 1987) is given as follows:

$$\eta' = \eta_s + \sum_{k=1}^{n_{mode}} \frac{\eta_{pk}}{1 + (\lambda_k \omega)^2} \tag{11a}$$

$$G' = \sum_{k=1}^{n_{mode}} \frac{\eta_{pk} \lambda_k \omega^2}{1 + (\lambda_k \omega)^2} \tag{11b}$$

which applies for all frequencies in the linear regime.

We again use this model because of the predicted normal stress generation, which is important in determining the thrust generation with polymer solutions. We limit the parameter ranges to $\eta_{pk} \in [0, \frac{5}{2}\eta_s]$, $\lambda_k \in [10^{-5}, 10^{-2}]$ (sec), and $\alpha_k \in [0.01, 0.5]$. The total number of design variables is $3k$, where k is the number of relaxation modes in the parameterization.

2.1.3 Parameters

Fluid properties, model parameters, computational mesh resolutions, operating conditions, and design constraint parameters for Cases 0, 1, and 2 in Table 1 are given in this section. The top and bottom discs (gap-controlled rotating disc and fixed textured surface in Fig. 1a–b) have the same outer radius (r_o) of 20 mm. The minimum controlled gap height between top and bottom discs (h_0) is 269 μm ; this value is used as the lower bound for the texture design gap height variable. The number of periodic sectors needed to construct a full disc (N_ϕ) is 10. The number of mesh nodes for each r -, θ -, and z -direction is $n_r = 6$, $n_\theta = 6$, and $n_z = 4$, respectively. Note that n_z does not apply to Case 1. The angular velocity of the flat plate (Ω), as shown in

Fig. 1a, is 10 rad/s; solvent viscosity (η_s) and density (ρ_s) values are 9.624×10^{-3} Pa·s and 873.4 kg/m³. The number of modes for the Giesekus fluid model is $n_{\text{mode}} = 2$ for Cases 1 and 2. For Case 0, this variable is not defined. The maximum angle for the texture inclination ($\theta_{\text{incl}} = 60^\circ$) is explained in Section 2.2.

2.2 Design problem formulation

The design problem considered here is the simultaneous minimization of the input power to the rotating flat plate and maximization of the load-supporting normal force, while constraining the maximum texture inclination angle. This problem is formulated as a constrained nonlinear optimization problem as follows:

$$\underset{\underline{x}_{\text{lb}} \leq \underline{x} \leq \underline{x}_{\text{ub}}}{\text{minimize}} \quad \underline{f}(\underline{x}) = [P, -F_N]^\top \quad \text{subject to:} \quad (12a)$$

$$\underline{g}_1(\underline{x}) = \left[\left| \frac{h_{kj} - h_{(k-1)j}}{r_k - r_{(k-1)}} \right|, \left| \frac{h_{il} - h_{i(l-1)}}{r_i \theta_l - r_i \theta_{(l-1)}} \right| \right]^\top$$

$$-\theta_{\text{incl}} \leq \underline{0} \quad (12b)$$

$$\underline{g}_2(\underline{x}) = -h_{n_r,1} + h_{n_r,l} \leq \underline{0} \quad (12c)$$

$$\underline{h}_3(\underline{x}) = h_{i1} - h_{in_\theta} = \underline{0}, \quad (12d)$$

where:

$$P = M\Omega \quad (12e)$$

$$F_N = N_\phi \int_{-\varphi/2}^{\varphi/2} \int_{R_i}^{R_o} (p|_{z=0} - \tau_{zz}|_{z=0}) r dr d\theta \quad (12f)$$

$$M = N_\phi \int_{-\varphi/2}^{\varphi/2} \int_{R_i}^{R_o} (r\tau_{\theta z}|_{z=0}) r dr d\theta \quad (12g)$$

$$p_{ij}, \tau_{ij} \leftarrow \text{flow-solver}(\underline{x}), \quad (12h)$$

for all $i = 1, \dots, n_r$, $j = 1, \dots, n_\theta$, $k = 2, \dots, n_r$, and $l = 2, \dots, n_\theta$. The design objectives are to minimize the power input $P = M\Omega$ and to maximize the normal force F_N simultaneously. Simultaneous optimization of the two objective functions (multiobjective optimization) results in a set of Pareto-optimal (nondominated) solutions. A manufacturability constraint applied in our previous study (Lee et al. 2017b) is also implemented via the first vector-valued inequality constraint function \underline{g}_1 . The maximum allowable local inclination angle between neighboring control points of the Lagrange polynomial interpolation over the texture geometry is limited to a predefined constant vector θ_{incl} . In addition, it is possible to have an infinite number of designs that are physically identical unless we set a reference point that is lower than any other location with the same radius, since the spatial design domain is rotationally periodic. To prevent this problem, we impose the inequality constraint $\underline{g}_2(\underline{x})$. Also, the periodic boundary condition in the spatial design domain is specified using the constraint $\underline{h}_3(\underline{x})$.

The design variable vector \underline{x} is comprised of both surface height values at mesh nodes, h_{ij} , and fluid model parameters associated with each viscoelastic relaxation mode, k , given as $\underline{x} = [h_{ij}, \eta_{pk}, \lambda_k, \alpha_k]^\top$ for all $i = 1, \dots, n_r$, $j = 1, \dots, n_\theta$, $k = 1, \dots, n_{\text{mode}}$, and assuming we have a given fluid viscosity η , used as $\eta(\dot{\gamma}_1 \approx 0) = \eta$ and $\eta_s = \eta$ for the Giesekus model. The texture design is represented by a curvilinear mesh fitted to the cylindrical coordinate system and nodes spaced according to Gauss-Lobatto-Legendre (GLL) points (Fornberg 2009) for each r - and θ -direction. Gap heights h_{ij} are defined for each node of the mesh, where i and j are indices of the nodes in r - and θ -directions. The texture design defined by h_{ij} is interpolated using Lagrange polynomials; the resulting texture surface used in this model is continuous and smooth. The viscoelastic material functions for the CEF model are described using analytical solutions of the material functions from the Giesekus model as described in Section 2.1.1. This representation strategy reduces the number of design variables significantly, which allows the same design variable set to be used for the two fluid models. Material functions used in the non-Newtonian fluid models are constrained to disallow certain combinations of values that are not numerically or physically realizable. This is implemented using the SVDD technique (Malak and Paredis 2010), and is discussed in Section 3.2.2.

3 Methodology

3.1 Solution procedures for fluid flow

3.1.1 Lower fidelity model: thin-film Reynolds equation with CEF fluid

Previously, we have developed code for solving the flow of an incompressible Newtonian fluid over general surface textures using the Reynolds equation (Schuh et al. 2017), and have used that code for optimization of textured surfaces (Lee et al. 2017b). A previous study (Ashmore et al. 2008) showed that viscoelasticity can be included in the thin-film governing equations using the CEF model.

Here, we derive a modified Reynolds equation with the CEF model for our design problem. Full details are provided in the [Supplementary Materials](#) and Schuh (2018). Briefly, we apply the following assumptions: (i) the gap height is small compared to the radius of the textured disk ($h(r, \theta)/R \ll 1$); (ii) shear rate ($\dot{\gamma}(r, \theta) = r\Omega/h(r, \theta)$) is independent of z , (iii) there exist no second normal stress difference coefficient ($\Psi_2 = 0$), resulting in pressure that does not vary in the z -direction ($\partial p/\partial z = 0$), and (iv) zero gradients in the z -direction are assumed for the other viscometric functions ($\partial \eta/\partial z = 0$, $\partial \Psi_1/\partial z = 0$). Splitting

the pressure and velocity fields into $p = p_0 + p_1$ and $\underline{u} = \underline{u}_0 + \underline{u}_1$, and applying appropriate boundary conditions for the velocity fields results in two equations governing the flow of a CEF fluid over general surface textures; an equation similar to the steady-state Reynolds equation may be given as follows:

$$\frac{1}{r} \frac{\partial}{\partial r} \left(\frac{r h^3}{12\eta} \frac{\partial p_0}{\partial r} \right) + \frac{1}{r} \frac{\partial}{\partial \theta} \left(\frac{h^3}{12\eta r} \frac{\partial p_0}{\partial \theta} \right) = \frac{1}{r} \frac{\partial}{\partial \theta} \left(\frac{r \Omega h}{2} \right), \tag{13}$$

which includes shear thinning, and another equation (where the right-hand side depends on the local Reynolds number and the local relationship between elasticity and viscosity) given as follows:

$$\frac{1}{r} \frac{\partial}{\partial r} \left(\frac{r h^3}{12\eta} \frac{\partial p_1}{\partial r} \right) + \frac{1}{r} \frac{\partial}{\partial \theta} \left(\frac{h^3}{12\eta r} \frac{\partial p_1}{\partial \theta} \right) = \frac{1}{r} \frac{\partial}{\partial r} (r G_r) + \frac{1}{r} \frac{\partial}{\partial \theta} (G_\theta), \tag{14}$$

where G_r and G_θ are functions of $r, h, \eta, \Psi_1, \frac{\partial p_0}{\partial r}$, and $\frac{\partial p_0}{\partial \theta}$. Detailed expressions for each term, and the full derivation of the modified CEF-Reynolds equations are given in Section 1 of the [Supplementary Materials](#) and in Schuh (2018).

3.1.2 Higher fidelity model: full 3-D momentum equation with Giesekus fluid

For the Giesekus model, the full Cauchy momentum equation is written in tensorial form as follows:

$$\frac{\partial \underline{u}}{\partial t} + (\underline{u} \cdot \nabla) \underline{u} = -\frac{1}{\rho} \nabla p + \frac{\eta_s}{\rho} \nabla^2 \underline{u} + \frac{1}{\rho} \nabla \cdot \underline{\underline{\tau}}_p, \tag{15}$$

where ρ is the fluid density, η_s is the solvent viscosity, and $\underline{\underline{\tau}}_p$ is the polymeric contribution to the shear stress. The contribution of the solvent has been pulled out of the stress tensor to improve numerical stability (Owens and Phillips 2002). We assume that the solvent and polymeric stresses add to produce the total shear stress:

$$\underline{\underline{\tau}} = \underline{\underline{\tau}}_s + \underline{\underline{\tau}}_p, \quad \underline{\underline{\tau}}_s = \eta_s \underline{\underline{\dot{\gamma}}}. \tag{16}$$

The governing equations (conservation of momentum and incompressibility (1a)) provide four equations with ten unknowns; therefore, a constitutive equation must be used for $\underline{\underline{\tau}}_p$ to solve the fluid flow system. As stated above, we are using the multimode Giesekus model given in (9) with $n_{\text{mode}} = 2$.

We solve the transient governing equations in cylindrical coordinates to steady state. The equations are solved on a periodic sector of a disk where $z \in [-h(r, \theta), 0]$; this is similar to our previous solution method with the Reynolds equation (Schuh et al. 2017; Lee et al. 2017b). The equations are discretized in space using a Galerkin pseudospectral method. We have mapped our 3-D periodic sector onto the $[-1, 1]$ cube using an invertible mapping (Deville et al. 2002; Kopriva 2009), where it

was assumed that the gradient of the gap height profile $h(r, \theta)$ exists everywhere in the computational domain. We use GLL quadrature with optimally chosen mesh points and quadrature weights so that the quadrature is exact for approximating polynomials of degree $2N - 1$, where $N + 1$ is the number of discretization points in a given direction (Heath 2002; Fornberg 2009). We use a third-order Adams Bashforth method with third-order extrapolation for the nonlinear terms in the time discretization. A velocity splitting technique is used for solving the pressure Poisson equation at each time step, and the diffusion terms are treated implicitly to aid stability (Owens and Phillips 2002).

The transient Cauchy momentum equations are solved with a maximum CFL number of 0.8, where the local CFL number is defined as $C = u \Delta t / \Delta x$. Each fluid parameter is constrained based on physical or numerical limitations as explained in Section 2.1.2.

3.1.3 Pseudospectral method

We solve both governing equations presented in Sections 3.1.1 and 3.1.2 using a Galerkin pseudospectral method for a periodic sector with $p_0|_{r=R_0} = p_1|_{r=R_0} = 0$, $\partial p_0 / \partial r|_{r=R_i} = \partial p_1 / \partial r|_{r=R_i} = 0$, and periodic boundary conditions in the θ direction. The Dirichlet boundary condition $p|_{r=R_0} = 0$ is used to match results described in Macosko (1994) for flow between parallel disks. We use N_D th order Lagrange polynomials for approximating quantities for each geometric dimension D . The texture design provided to the flow simulation is represented by the gap height h_{ij} for $i, j = 1, \dots, n_r$, and the solution procedure associated with the pseudospectral method assumes that the entire computational domain is continuous and smooth in Lagrange polynomial form. Thus, this method obtains a very accurate fluid flow solution, even for coarse spatial meshes. Solutions for the design problem will also be smooth and continuous in the form of a Lagrange polynomial. Also, by maintaining the same mesh for the design representation and the simulation domain representation, we obtain very accurate design solutions without requiring a large number of design variables due to the characteristics of the interpolating polynomials used in the pseudospectral method. Increasing the mesh density, however, may introduce new practical design complexities, such as thinner texture features on the surface.

3.1.4 Experimental validation of numerical models

The lower fidelity model (thin-film Reynolds equation with CEF fluid) and the higher fidelity model (full 3-D momentum equation with Giesekus fluid) are validated against steady shear experiments for varying concentrations of PIB in mineral oil (trade name S6) using a cone-and-plate rheometer

geometry of $\Theta=1.011^\circ$ and $R=20$ mm, where Θ and R denote the cone angle and the radius, respectively. The comparison results show good agreement between both high and low fidelity models in steady state and between numerical and experimental results. The detailed comparisons of the raw torque and the raw normal thrust between experimental data and simulation results are provided in Section 3 of the [Supplementary Materials](#).

3.2 Design procedures

3.2.1 Multiobjective adaptive surrogate modeling-based optimization (MO-ASMO)

Efficient and effective sampling strategies for surrogate modeling-based optimization (SMBO) are well-studied in the context of finding a single optimum by balancing exploration and exploitation objectives in constructing surrogate models (Wang and Shan 2007). However, studies of sampling strategies for multiobjective optimization problems (MOPs) are largely limited to a global level improvement of surrogate model accuracy as opposed to more efficient targeted accuracy improvements (Wilson et al. 2001; Steponavičė et al. 2016). Shan and Wang (2004) developed the Pareto set pursuing (PSP) methodology that generates new training points toward regions where the predicted Pareto set is located, resulting in significant improvements in computational efficiency for solution of MOPs using SMBO.

The multiobjective adaptive surrogate modeling-based optimization (MO-ASMO) strategy used here (Lee et al. 2017a) is a surrogate-based optimization framework that can manage multiple objective functions, tens or hundreds of design variables, and multiple linear and nonlinear constraints. Figure 2 illustrates a high-level process description for this type of algorithm (direct sampling Wang and Shan 2007). We have developed this method primarily for solving problems with complicated constraints that result in narrow or otherwise difficult to navigate feasible domains. It avoids infeasible samples to reduce inefficient use of high-fidelity simulations, especially designs that are not physically meaningful or that result in numerical

instability. The method aims to balance choosing samples that help improve surrogate model accuracy in the vicinity of the Pareto-optimal solution (a hypersurface in the design space), with choosing samples that aid exploration to improve the probability of finding global optima. The problem considered here is well-matched for this MO-ASMO method as it involves a large number of constraints that interrelate multiple design variables, and a computationally expensive simulation. Readers are referred to Lee et al. (2017a) for a detailed description of this method, including sampling and validation, as well as openly available source code.

3.2.2 Feasibility management using support vector domain description (SVDD)

When using simulations that use design variables as inputs, it is possible that certain combinations of design variable values correspond to a physically meaningless design that results in simulation failure. Some combinations that are physically meaningful may also result in numerical instabilities and simulation failure. In some cases, it may be possible to prevent consideration of designs that cause simulation failure via explicit algebraic constraints (Lee et al. 2017a). In other cases, it may not be known what variable combinations may cause failure until attempting simulation, preventing definition of constraints a priori. In these circumstances, an alternative strategy is required.

In the studies presented here, it is not possible to define constraints a priori that prevent simulation failure. Certain numerical instabilities arise for a range of different designs. A strategy was developed to define arbitrary constraint boundaries (nonconvex, disconnected infeasible domains) adaptively based on observed failed simulations. This strategy is based on SVDD (Tax and Duin 1999; Malak and Paredis 2010). In earlier work, SVDD was used to define complex feasible regions. Here, SVDD is used in the opposite manner to define regions of points that are infeasible in the sense that they lead to simulation failure. Availability of these constraints helps to avoid wasteful consideration of points that cannot be simulated.

At each MO-ASMO main iteration, the SVDD approximation of regions that cannot be simulated is improved by adding newly discovered infeasible points to the SVDD dataset. Using a strategy that defines the infeasible domain rather than the feasible domain avoids excessive limitations on design space exploration, all without a priori knowledge of the regions that cannot be simulated.

We constructed the Gaussian kernel-based SVDD (Tax and Duin 1999) using a maximization problem given as follows:

$$\underset{0 \leq \beta \leq C}{\text{maximize}} \quad W(\underline{\beta}) = \sum_i \beta_i K_G(\underline{x}_i, \underline{x}_i) - \sum_{i,j} \beta_i \beta_j K_G(\underline{x}_i, \underline{x}_j), \quad (17)$$

where \underline{C} is a vector of appropriate length where each element is the constant C . The Lagrange multipliers $\underline{\beta}$ are

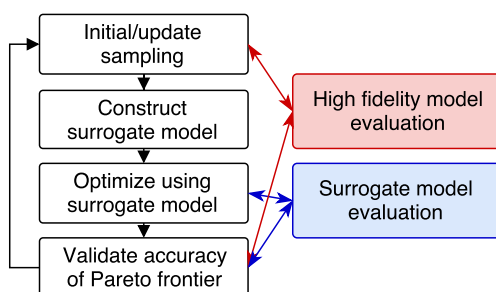


Fig. 2 Flow chart illustrating the MO-ASMO framework with direct sampling method (Lee et al. 2017a; Wang and Shan 2007)

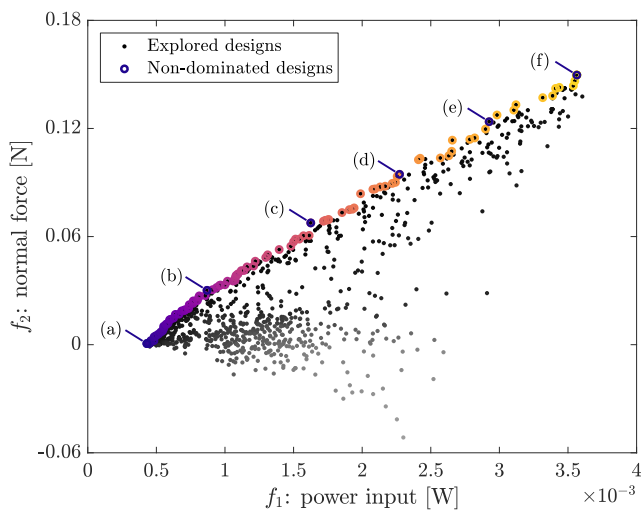


Fig. 3 Explored designs and optimal solutions (nondominated designs) for the CEF model, Case 1, displayed in the objective function space

bounded above by \underline{C} . Varying C can help detect the outliers in the dataset that describes the domain. $K_G(\cdot, \cdot)$ is the Gaussian kernel function. After we construct the domain using the SVDD, an arbitrary point \underline{z} is inside the described boundary if:

$$R^2(\underline{x}) - R^2(\underline{z}) = K_G(\underline{x}, \underline{x}) - K_G(\underline{z}, \underline{z}) + 2 \sum_i \beta_i (K_G(\underline{z}, \underline{x}_i) - K_G(\underline{x}_i, \underline{x}_i)) \geq 0, \quad (18)$$

where \underline{x} is a bounding point, which is called a support vector. A detailed explanation of SVDD is provided in Section 2 of the [Supplementary Materials](#).

4 Results and discussion

4.1 Case 1: Lower-fidelity model with CEF fluid

Solutions of design problem Case 1 (CEF model with Reynolds equation) are illustrated in the objective function

space in Fig. 3. Since the objective functions are (i) to minimize the power input and (ii) to maximize the normal force, we desire points in this space to be close to the top-left corner. We used the Gaussian process surrogate modeling technique within the MO-ASMO framework for all numerical optimization studies presented here. Among the several stopping conditions available, we selected an average error criterion (less than 1%) evaluated during the validation stage in the MO-ASMO for terminating the optimization process. Optimal solutions (in the form of a Pareto frontier) are marked with colored circles, whereas all other design points evaluated during the course of optimization are marked with black- and gray-scale dots. If a design point is displayed in a darker gray than another, this indicates that the former dominates the latter. Points having the same gray-scale intensity means they have the same rank according to a nondominated sorting strategy (Deb et al. 2002). Optimal solutions have a range of input power values from 4.31×10^{-4} to 3.56×10^{-3} [W], and a range of normal force values from 6.16×10^{-4} to 1.50×10^{-1} [N]. The labels (a) through (f) that identify specific marked points in Fig. 3 correspond to the texture and fluid designs given in Fig. 4a–f and plot legends (a)–(f) of Fig. 5a, b. These representative solutions (a) through (f) were chosen subjectively based on the following criteria: (i) they should not be located in close proximity in the objective function space; (ii) they should be among the best solutions in the Pareto frontier, i.e., they should be a point closer to the utopia point among solutions in close proximity; (iii) and they should be evenly distributed in the objective function space.

Design result (a) for Case 1 (refer to design point (a) in Figs. 3, 4a, and Line (a) in Fig. 5a) is an anchor point of the Pareto set; it has the minimum power value over all feasible designs. An anchor point is a nondominated point with one of the objective functions optimized, with all other objective functions ignored. Design point (a) results when power is minimized and normal force is not considered.

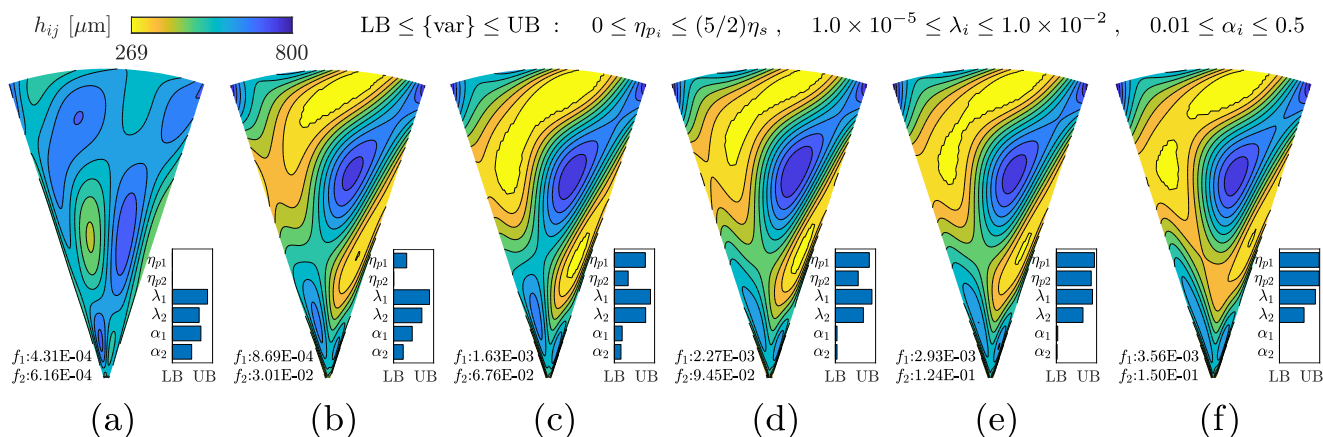


Fig. 4 Sample textured sector and fluid designs in the Pareto set from the CEF model case: f_1 represents the first objective function (power input [W]) and f_2 represents the second objective function (normal force [N])

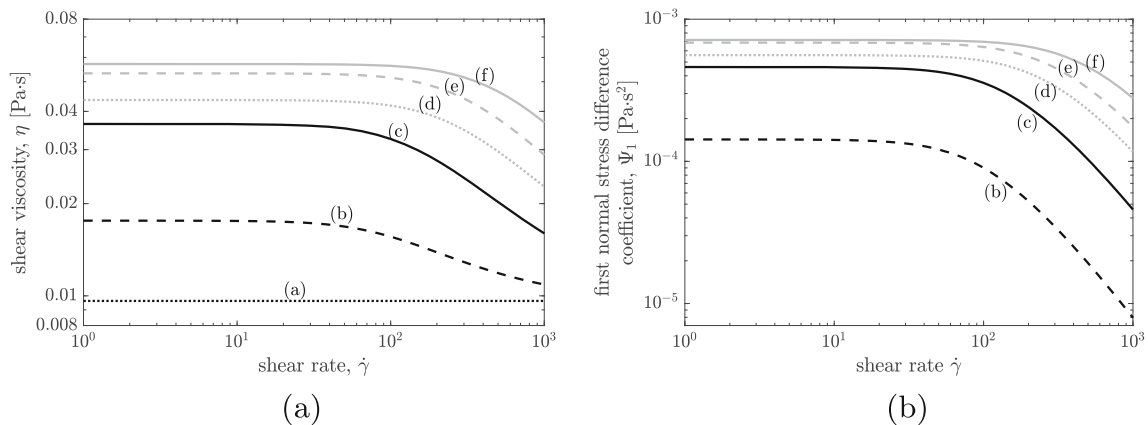


Fig. 5 Viscoelastic material functions of corresponding sample optimal designs from the CEF model case. **a** Shear viscosity; **b** first normal stress difference coefficient. Curves (a)–(f) correspond to designs (a)–(f)

This minimum power design exhibits a relatively flat texture surface with a small amount of asymmetry, and does not generate much normal force (4.31×10^{-4} [N]). This design solution is Newtonian (e.g., no polymer additive) and shows a flat shear viscosity in Line (a) of Fig. 5a, since the polymer viscosity values have converged to zero for all modes. Necessarily, no first normal stress difference appears.

Design result (f) (refer to design point (f) in Figs. 3, 4f, and Line (f) in Fig. 5a and b) is the other anchor point, which has a maximum normal force without consideration of power input. Unlike the former anchor point, this design has strong asymmetry with distinct elevation changes in the texture to form a spiral blade-like shape. As explained in our previous study, this spiral texture design directs the fluid pressure radially inward by acting as a converging channel, eventually generating the positive net normal force due to increased pressure near the disc center (Lee et al. 2017b). Also, this design solution includes non-Newtonian fluid properties with high polymer viscosity values for both modes (η_{p1} and η_{p2}). High polymer viscosity lifted the plateau of the overall shear viscosity as shown in Line (f) of Fig. 5a and has the highest first normal stress difference values for the entire shear-rate regime, as shown in Line (f) of Fig. 5b. These results are congruent with earlier studies based on Newtonian fluids where it was observed that (i) a deeper surface reduces frictional loss, (ii) symmetric surfaces do not generate any normal force due to geometric properties, and (iii) stronger asymmetry generates larger normal forces (Lee et al. 2017b; Schuh et al. 2017).

Other designs on the Pareto frontier between these two anchor points (refer to design points (b)–(e) in Figs. 3 and 4b–e) have consistent trends. Specifically, we observe that (i) the general shape of the surface texture designs does not change significantly, but steeper inclines in the texture are required to generate higher normal forces, and (ii) an increased polymer viscosity and a decreased nonlinearity

in Figs. 3 and 4. Increased viscoelasticity (e.g., polymer additive) appears in designs (a)–(f)

(anisotropy described by the mobility factor) help obtain higher normal forces.

These results show that the nonlinearity mainly plays a role when we optimize both objective functions simultaneously. An increased polymer viscosity tends to help increase load capacity, and increased nonlinearity helps reduce frictional losses. It should be noted that these responses are non-monotonic and have optimum values for achieving a certain balance between the two objectives.

To quantify the numerical solver uncertainty, solver parameter sensitivities were analyzed at the six selected solution points identified as (a)–(f) in Fig. 3. The solver parameter sensitivities are computed by obtaining deviations in the objective function values with predictable deviation possibilities in parameters, such as radius of the rotating disc (R_o), minimum controlled gap height between

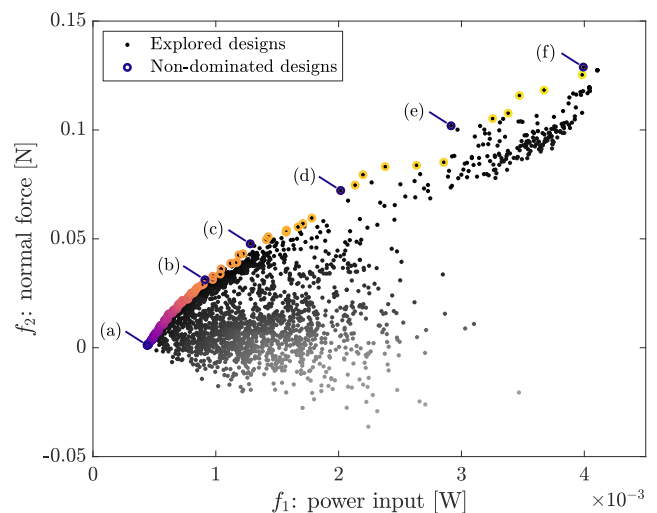


Fig. 6 Explored designs and optimal solutions (nondominated designs) for the multimode Giesekus model, Case 2, in the objective function space

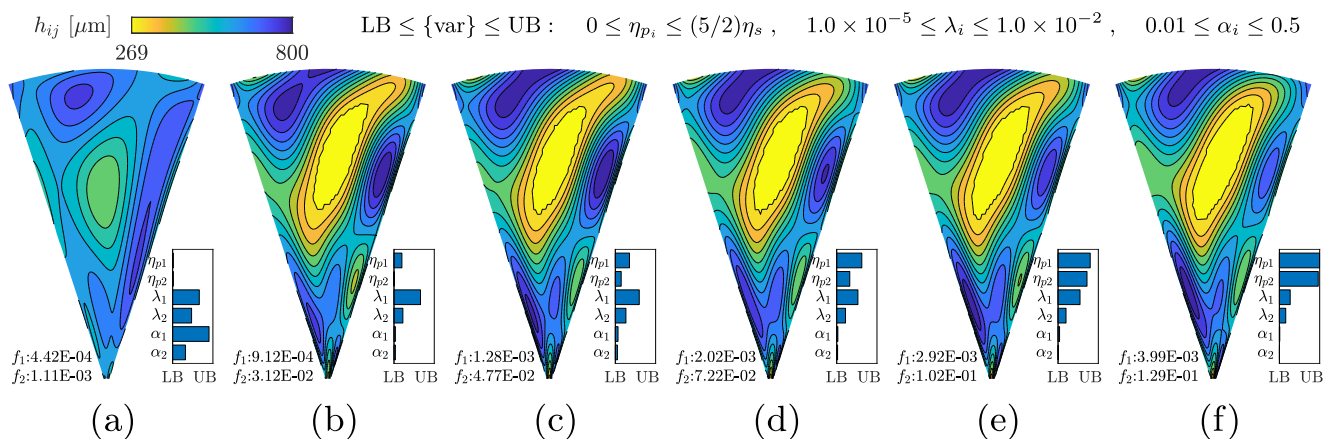


Fig. 7 Sample textured sector and fluid designs in the Pareto set from the multimode Giesekus model case: f_1 represents the first objective function (power input [W]) and f_2 represents the second objective function (normal force [N])

discs (h_{min}), angular velocity of rotating disc (Ω), solvent viscosity (η_s), and solvent density (ρ_s), using the differential sensitivity analysis method. Deviations in parameters R_o and ρ_s affect less than 1% in both objective functions. Deviations in parameters Ω and η_s make changes between 1 to 3% in either or both objectives. Thus, this numerical solver is reliable for these four parameters. However, a deviation in h_{min} results in approximately 4% change in the first objective (power input) and about 11% change in the second objective (normal force). Thus, removing the offset in the gap height between discs is very important specifically for maintaining accuracy in normal force prediction. Detailed sensitivity analysis results are given in Table 1 in Section 4 of the [Supplementary Materials](#).

4.2 Case 2: Higher fidelity model with Giesekus fluid

Solutions of the design problem Case 2 (multimode Giesekus model with transient Cauchy momentum equation) are illustrated in the objective function space in Fig. 6.

As with the CEF model (Fig. 3), the direction of desired performance is toward the top-left corner, and the labeling strategy is kept consistent. Optimal solutions have a range of power input from 4.42×10^{-4} to 3.99×10^{-3} [W], and a normal force range of 1.11×10^{-3} to 1.29×10^{-1} [N]. The labels (a) through (f) indicate specific non-dominated points in Fig. 6 that correspond to the texture and fluid designs shown in Fig. 7a–f and plot legends (a)–(f) of Fig. 8a, b.

Design result (a) of Case 2 (refer to design point (a) in Figs. 6 and 7a, and Line (a) in Fig. 8a) is the anchor point with minimum power input. This design shows a relatively flat texture surface with a small amount of asymmetry and Newtonian fluid properties, as was observed in Case 1. The maximum normal force anchor point is design point (f) in Fig. 6 (also in Fig. 7f and Line (f) in Fig. 8a, b). This design has the most distinct elevation changes in the texture, and, similar to the previous case, forms a spiral blade-like shape. As we see in Case 1, this design has the second highest plateau value in shear viscosity as shown in Fig. 8a and the high first normal stress difference value as shown

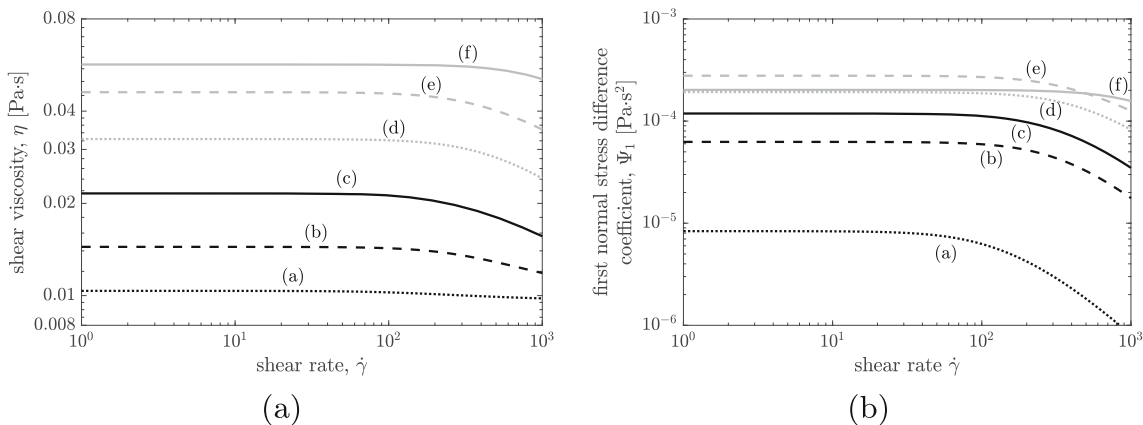


Fig. 8 Viscoelastic material functions of corresponding sample optimal designs from the Giesekus model case. **a** Shear viscosity; **b** first normal stress difference coefficient. Curves (a)–(f) correspond to

designs (a)–(f) in Figs. 6 and 7. Viscoelasticity (e.g., polymer additive) generally increases in designs (a)–(f)

in Fig. 8b. As observed in these results, having a larger first normal stress difference at a higher shear rate has a more significant impact on generating overall normal force than when operating in a lower shear-rate regime. Although flow described by the Giesekus model can exhibit second normal stress difference (Ψ_2) effects, the results show that magnitudes of Ψ_2 are at least 1 to 2 orders of magnitude smaller than Ψ_1 and do not contribute a meaningful amount of normal force generation.

Other designs on the Pareto frontier between these two anchor points (refer to design points (b)–(e) in Figs. 6 and 7b–e) also exhibit consistent trends: (i) the surface texture shapes do not change significantly, but larger elevation changes are needed to acquire higher normal forces; (ii) an increased polymer viscosity is associated with higher normal forces; and (iii) the nonlinearity (mobility factor) is maintained with low (but nonzero) values for the entire range of designs.

Thus, for Case 2, we can observe an increase in the normal force with a simultaneous increase in the power input as polymer viscosity values in modes 1 and 2 increase (from design (b) through (f)). However, all the optimal solutions converged to low mobility factor values, suggesting that shear thinning is not desirable. Also, the optimal textures from Case 2 are in general deeper than those for Case 1. Design point (f) in Fig. 8b shows a different trend when comparing to other design points in Case 2 or Case 1. Even though Ψ_1 is lower in (f) than in (e), it produces a larger normal force. This is because the normal force is the integral of the normal stress difference times the squared shear rate over the entire textured domain. At the higher shear-rate values, (f) is larger than (e), resulting in a larger contribution to the normal force. This is consistent with the notion that shear thinning in the normal stress differences decreases the normal force. Therefore, other designs not considered here that keep the shear thinning profile for the viscosity while having a nearly constant Ψ_1 across the desired shear-rate range may produce better lubrication results.

To quantify the numerical solver uncertainty, solver parameter sensitivities were analyzed at the six selected solution points identified as (a)–(f) in Fig. 6. The solver parameter sensitivities are computed using the same procedure described in Section 4.1. Deviations in parameters R_o and ρ_s produce up to 1% differences in both objective functions. Deviations in parameters Ω and η_s make changes between 1 and 3% in either or both objectives. With these results, we can conclude that this numerical solver is reliable for these four parameters. However, a deviation in h_{\min} produces up to 5% change in the first objective (power input) and about 10% change in the second objective (normal force). Thus, as we concluded earlier, removing the offset in the gap height between discs

is very important for maintaining accuracy in normal force prediction. Detailed sensitivity analysis results are given in Table 2 in Section 4 of the [Supplementary Materials](#).

4.3 Case 0: Newtonian fluid model case result

An additional study is performed here using a Newtonian fluid model with a transient Cauchy momentum equation to provide a reference solution (Case 0). Solutions of this case are shown in Fig. 9. Optimal solutions have a range of power input from 3.43×10^{-4} to 6.73×10^{-4} [W], and a range of normal force values from 1.45×10^{-4} to 2.51×10^{-2} [N]. The labels (a) through (f) indicating specific marked points in Fig. 9 correspond to the texture and fluid designs given in Fig. 10a–f.

Similar to the results obtained from the non-Newtonian fluid studies, we see analogous trends in the shape of the surface textures. An anchor point with a minimum power input (shown as design point (a) of Case 0) has a deep and relatively planar textured surface. The maximum normal force anchor point, shown as design point (f), has a sharp and distinct asymmetric spiral blade-like texture shape, which directs the fluid pressure radially inward to generate a positive net normal force.

Other designs on the Pareto frontier between these two anchor points (refer to Points (b)–(e) in Figs. 9 and 10b–e) have a consistent trend; unlike the other two non-Newtonian fluid cases, the texture designs are notably different from each other. The optimal designs on the Pareto frontier in this case show how changes in texture design only impact generated normal force values since all the designs have the same Newtonian fluid properties. Comparatively, sudden elevation changes in the texture are observed for the entire

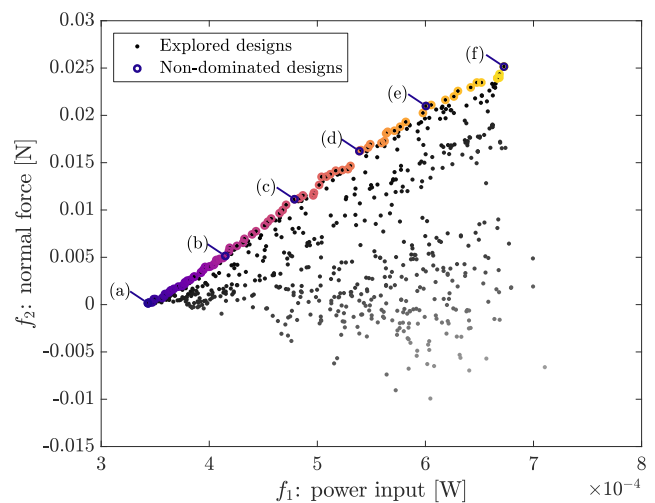


Fig. 9 Explored designs and optimal solutions (nondominated designs) for the Newtonian fluid model, Case 0, in the objective function space

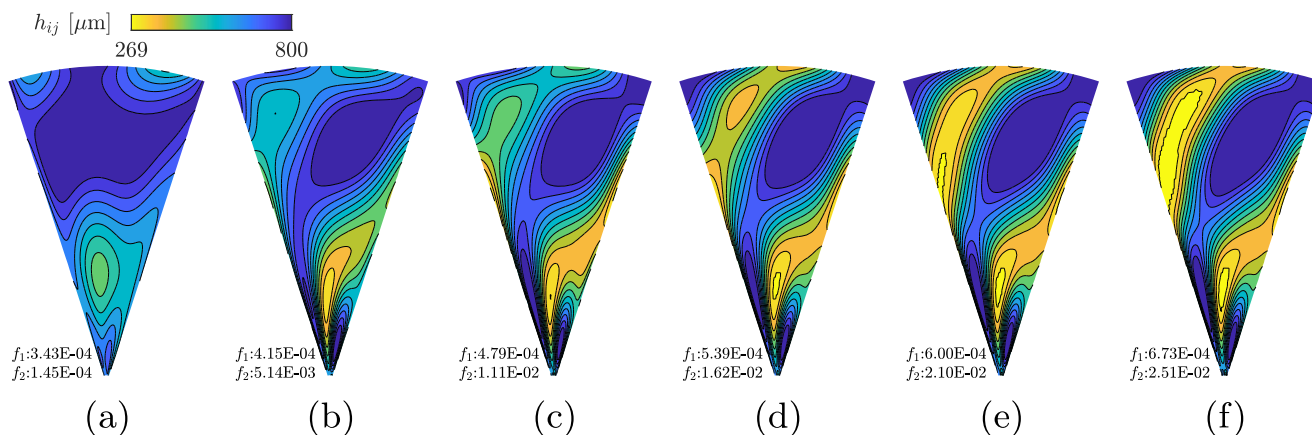


Fig. 10 Sample textured sector designs in the Pareto set from the Newtonian fluid model case: f_1 represents the first objective function (power input [W]) and f_2 represents the second objective function (normal force [N])

set of design points that generate normal force (specifically see design points (b)–(f)).

4.4 Comparisons and discussion

4.4.1 Pareto set comparison

Figure 11 shows Pareto sets for three design studies simultaneously, including CEF (Case 1), Giesekus (Case 2), and Newtonian fluid model (Case 0) studies. Dots represent Pareto-optimal solutions (design points) in the objective function space, while circles represent the corresponding utopia points for each of the three design studies.

The study based on the Newtonian fluid model serves as a reference, illustrating how much normal force can be generated through improved texture design alone without tailoring non-Newtonian effects. For Newtonian fluids, Pareto-optimal designs span only a small range of power input levels (from 3.43×10^{-4} to 6.73×10^{-4} [W]). The

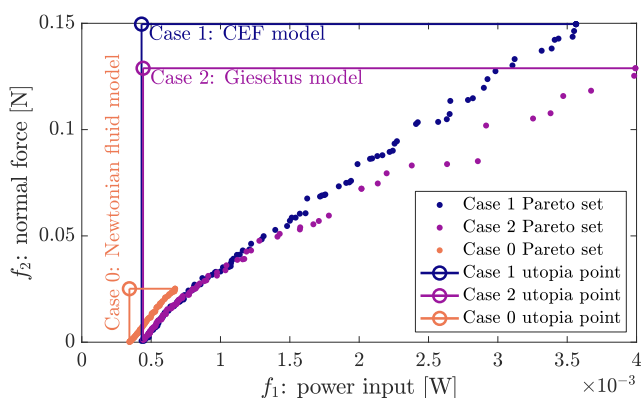


Fig. 11 A comparison of the optimal solutions (Pareto set) of CEF, Giesekus, and Newtonian fluid models in the objective function space

maximum possible normal force generated without aid from viscoelastic effects is 2.51×10^{-2} [N].

When parameters that define fluid properties are added as design variables, the maximum possible normal force generated is increased by a factor of six. The CEF model case exhibits a maximum possible normal force of 1.50×10^{-1} [N], with a corresponding power input of 3.56×10^{-3} [W]. Using the multimode Giesekus model, we can obtain a maximum normal force of 1.29×10^{-1} [N], with a corresponding power input of 3.99×10^{-3} [W]. Although we used the same parameterizations for designing fluids in both non-Newtonian fluid cases, we see a significant difference in normal force generating capability. Design based on more simplified fluid simulations (i.e., modified Reynolds equation using a CEF fluid model) demonstrated the ability to identify designs that generate higher normal force values, at least as predicted by these simplified models.

4.4.2 Analysis of friction reduction and load-supporting normal force

As we see in Figs. 3, 6, and 9, the two objectives of decreasing the input power and increasing the normal force are competing. When trying to minimize the input power, the optimal solutions indicate no added polymer (resulting in base solvent viscosity) and have the deepest texture profiles that result in the smallest shear stress. However, when aiming to maximize the normal force produced, the optimal solutions have polymer additives and exhibit a spiral-shaped texture profile. Designing the fluid parameters in this region is a nontrivial task, in part due to nonmonotonic relationships between the normal force and the viscoelastic design parameters. This suggests that optimization of the viscometric functions plays a key role in a performance enhancement.

4.4.3 Model comparison

Based on the above results, the two fundamental problem types are (i) simultaneous design of texture and fluid properties and (ii) design of texture-only with fixed fluid properties.

While the simultaneous texture and fluid design problem was solved using two distinct numerical fluid simulation models, they correspond to the same physical design problem. Both cases involve using a viscoelastic fluid (polymeric solution) as the lubricant, designing the fluid properties, and designing the texture shape. The only difference between these two cases is how the behavior was predicted, and the simplifying assumptions made. We highlight this point to clarify that the decision between methods can instead be made based on the following criteria: (i) computational efficiency, (ii) prediction accuracy, (iii) range of numerical limits, and (iv) range of types of fluid behaviors that the model can predict. The models are compared here along these dimensions.

First, the CEF-Reynolds equation has a very efficient computational structure; the entire optimization using the MO-ASMO algorithm took only 21 min, whereas direct optimization using the NSGA-II algorithm required 85 min, both computed using a dual Xeon Gold 6130 workstation with 64 computing threads. The steady-state solution can be obtained directly without using a time-marching transient solution procedure. Also, the CEF-Reynolds equation can predict the pressure and stress of the flow field efficiently within assumptions made during derivation. Since the CEF model can include shear-rate dependent viscosity and normal stress differences in calculating the velocity and pressure fields, the nonlinear viscoelasticity observed in our polymeric lubricant can be predicted well. However, because of the assumptions and limitations underlying the CEF-Reynolds equation (see Section 3.1.1 and Schuh 2018), prediction accuracy may be poor when certain flow conditions are present, such as recirculation or flow with nontrivial inertial effects. The CEF model maps material parameters to material properties in a less-constrained way compared to higher fidelity options. This additional flexibility results in a wider exploration of designs in the material property space and higher normal force values, but may result in properties that are more difficult to realize physically. Within the design ranges of the other models (power input up to 2.5 [W] and normal force up to 0.1 [N]), this model produces a Pareto frontier that mostly overlaps with the Pareto frontiers generated using the other models.

Second, the Cauchy momentum equation with a multi-mode Giesekus model is the most computationally expensive choice, but it can predict the fluid flow very accurately, including inertial effects, recirculation, and other 3D effects. The Giesekus model can also include shear-rate dependent

viscosity and normal stress difference effects on the velocity and pressure fields. Thus, this model is the most ideal for complex flow phenomena with nonlinear viscoelasticity. However, due to numerical instability under certain conditions, a particular set of input (shape and fluid) parameter values cannot be evaluated with this solver. Our MO-ASMO algorithm can handle these “unable-to-obtain-result” points by utilizing feasible region management functions based on a SVDD strategy. Thus, we improved computational solution efficiency by avoiding training samples that were incompatible with the model. After addressing this issue, the MO-ASMO algorithm produced improved solutions. However, even with the efficient MO-ASMO algorithm, the computation time for this optimization problem was significant (14 h using the same machine). The Pareto frontier for this case overlaps with the CEF model results, but it could not produce designs with comparably high normal force generation.

It should be noted that the performance metric values reported in these results are based on distinct model types. One approach to provide a more fair comparison would be to evaluate Pareto-optimal designs generated by the lower fidelity approaches via the higher fidelity Giesekus model. This was attempted, and unfortunately a number of nondominated solutions from the Case 0 and 1 approaches resulted in numerical instabilities. Related ongoing work involves experimental testing of the associated designs to provide an accurate and fair design method comparison, but this experimental work is outside the scope of this article. When these ongoing studies are concluded, more complete statements can be made regarding the behavior and utility of the design methods presented, and whether modifications could be made to the Case 1 approach to focus design exploration on realizable high-performance designs.

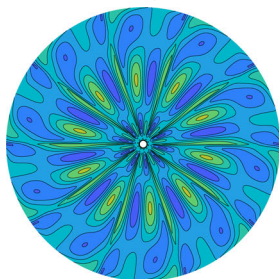
4.4.4 Texture shape comparison

Sample texture shapes of full discs from our design solutions are compared in Fig. 12. Texture designs from the CEF model case are shown in Fig. 12a, d, g; texture designs from the Giesekus model case are shown in Fig. 12b, e, h; texture designs from the Newtonian fluid model case are shown in Fig. 12c, f. Sample textures given here are selected to compare the resulting optimal textures between different fluid model cases.

Designs are arranged such that the normal forces generated by each design in a given row is similar. The first row designs (Fig. 12a, b, c) are the textures that generate nearly zero normal forces. These surface texture designs are relatively flat with a limited amount of asymmetry. The second row designs (Fig. 12d, e, f) are the textures that generate normal forces on the order of 3×10^{-2} [N]. These surface texture designs have very sharp and large

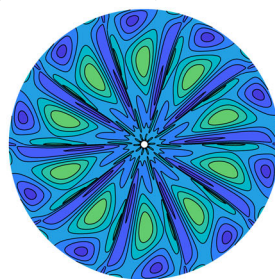
Fig. 12 Sample textured disc designs in the Pareto set from all three fluid model cases: f_1 represents the first objective function (power input [W]) and f_2 represents the second objective function (normal force [N]). **a, d, g** Results of CEF model case; **b, e, h** results of Giesekus model case; and **c, f** results of Newtonian fluid model case. **a, b, c** Generates nearly zero normal force; **d, e, f** generates normal force of $O(3E-02)$; and **g, h** generates normal force over $O(1E-01)$, which is not available with the Newtonian fluid

Texture of Fig. 4(a) design
 $f_1=4.31E-04, f_2=6.16E-04$



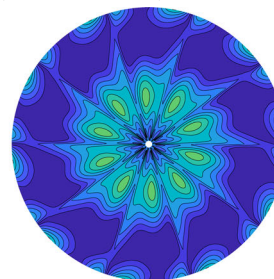
(a)

Texture of Fig. 7(a) design
 $f_1=4.42E-04, f_2=1.11E-03$



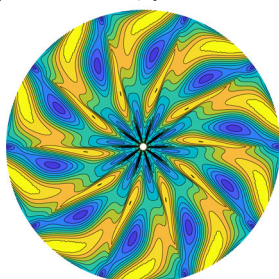
(b)

Texture of Fig. 10(a) design
 $f_1=3.43E-04, f_2=1.45E-04$



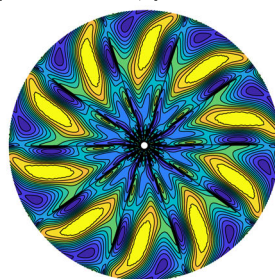
(c)

Texture of Fig. 4(b) design
 $f_1=8.69E-04, f_2=3.01E-02$



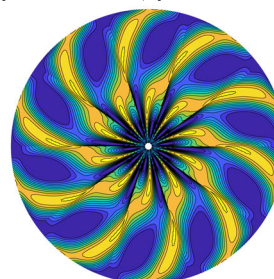
(d)

Texture of Fig. 7(b) design
 $f_1=9.12E-04, f_2=3.12E-02$



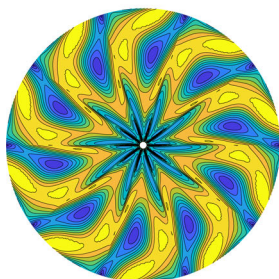
(e)

Texture of Fig. 10(e) design
 $f_1=6.00E-04, f_2=2.10E-02$



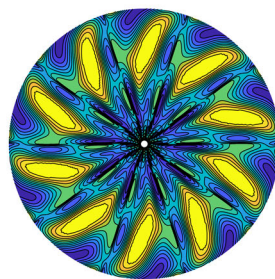
(f)

Texture of Fig. 4(f) design
 $f_1=3.56E-03, f_2=1.50E-01$

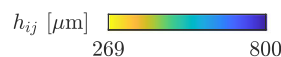


(g)

Texture of Fig. 7(f) design
 $f_1=3.99E-03, f_2=1.29E-01$



(h)



elevation changes to create a spiral blade-like pattern as discussed in Sections 4.1–4.3. For the Newtonian fluid model case, which relies on the texture to generate a normal force, the resulting design (Fig. 12f) generates a normal force value close to the highest possible without non-Newtonian fluid behavior. The third row (Fig. 12g, h) are the textures that generate normal force values over 1×10^{-1} [N], and are the highest normal force values for each of the respective design problems. Texture designs are not significantly different from the designs in the second row. This observation indicates that normal forces higher than what was purely achievable through only texture design depends solely on viscoelasticity. Further design studies using sequential design strategies (texture design

optimization followed by fluid design, or vice versa) rather than simultaneous design may provide stronger evidence for the effects of viscoelasticity on normal force generation.

As described in Section 4.4.3, each simultaneous texture and fluid design study (Cases 1 and 2) used the same design objectives and variables. In other words, they involve the same design formulation, but use different numerical simulation approaches for prediction. Thus, unless two different solution sets provide the exact same objective function values, one of these two sets of solutions may dominate the other. However, it is possible that multiple solutions exhibit almost identical performance values. This issue is connected to the question of which fluid model or fluid solver can predict the behavior more accurately. A

cross-validation of one solution with different fluid models, as well as an experimental validation of the solution, is needed and is a topic of ongoing work.

4.4.5 Problem formulation discussion

As we discussed earlier in Section 1, combined optimization of both fluid and surface texture in the lubricated sliding contact has not been considered previously. Thus, earlier efforts do not exist that could be used to build upon or compare to. The simultaneous problem formulation decisions were based on the discretion of the authors. In addition to the simultaneous approach used here, other problem formulations could be considered, such as sequential and nested approaches. It is known that the conventional sequential design process may not produce system-optimal solutions, while the nested and the simultaneous design approaches can identify system-optimal designs (Deshmukh and Allison 2016). The nested design method generally demands more computational expenses to the simultaneous design method. However, the nested design may outperform the simultaneous design approach if the following conditions exist: (i) when the dimension of the design problem is not small and (ii) when the inner-loop subproblem can be solved efficiently (Herber and Allison 2019). In this study, on the other hand, two different design targets (fluid and texture) are solved in a single simulation routine (one of the solvers presented in Section 3.1). Consequently, separating these two design targets into inner and outer loops is computationally inefficient, although formulating the design problem as a single optimization problem results in a large number of design variables.

While selecting a simultaneous formulation had clear benefits, determining an effective design representation for the fluid material functions was less straightforward. Using the Giesekus fluid parameterization for designing the material functions limits the solution within certain types of complex fluids. Using the Giesekus fluid parameterization does not mean that the solution fluid is only achieved by the polymeric additives; the same solution may be achieved via multiple different chemical and molecular formulation strategies. However, using a different class of fluids may result in fluid properties that cannot be realized by the Giesekus fluid parameterization. Investigating a variety of fluid parameterizations is beyond the scope of this study, but is an important open research question, and foundational work has been performed recently in several areas, including organizing different models for design (Ewoldt 2014), model selection studies (Freund and Ewoldt 2015), and database descriptions of complex rheological properties (Nelson and Ewoldt 2017).

5 Conclusion

In this study, we designed non-Newtonian lubricant properties and surface texture simultaneously for lubricated sliding contact using the MO-ASMO algorithm and two non-Newtonian fluid models. The Giesekus fluid parameterization used for both constitutive models provides practical and physically achievable material function shapes, but it is acknowledged that this parameterization strategy may limit fluid system design performance. Different models and design representations would be required to explore such an expanded design space, but would likely come at the cost of increased solution complexity and computational expense. We obtained nondominated optimal design solutions (i.e., Pareto sets) and compared a set of sample texture and fluid design results. We identified trends in texture shapes, which agreed with trends from our previous studies, observed fluid parameter trends, and identified how fluid design influences objective function values.

The MO-ASMO algorithm was applied successfully to solve this simultaneous fluid and texture design problem with two objectives. A direct optimization (using either nonlinear programming (NLP) or genetic algorithms) was impractical given our computational resources (specifically for Case 2). The MO-ASMO algorithm enables accurate solution without requiring access to exceptionally high-performance computing resources. A specific challenge arises when attempting to use general-purpose NLP algorithms due to the Giesekus model stability properties. Certain combinations of texture shape and fluid parameter values cause model divergence. An explicit and precise description of the boundary between compatible and incompatible parameter values is not available, making direct application of standard NLP solvers impractical. The MO-ASMO algorithm mitigates these issues effectively using the SVDD strategy for adaptively constructing an explicit boundary between regions with acceptable input values and those that lead to divergence. Our use of the SVDD strategy is differentiated from others by encapsulating observed invalid input regions to avoid during the exploration stage, which ensures a comprehensive exploration of the entire computable design space.

We observe that added viscoelasticity to the Newtonian solvent significantly increases normal force generation from the numerical optimization results in this study. All the optimal texture designs are qualitatively similar in shape to our earlier studies based on a Newtonian lubricant, but viscoelasticity plays a vital role in increasing normal force generation by up to a factor of 5 without a significant change in texture design. We see that optimal textures obtained with Newtonian and non-Newtonian fluids resulted in different

shapes and elevation changes. This shows that simultaneous design of the non-Newtonian lubricant and surface texture is necessary to achieve overall higher system performance.

A comprehensive set of physical experiments to compare performance indices (power input and normal force) for a carefully selected set of numerically optimized texture and fluid designs is a topic of ongoing work. Preparation for the experimental measurement requires microfabrication of textured discs and formulation of viscoelastic lubricants. Observing that all the design solutions on the Pareto frontier have different fluid properties, a set of representative sample designs will need to be selected carefully for comparison with simulation results. Experimental texture fabrication, fluid formulation, and testing are outside the scope of this article, which is focused on simulation-based optimization studies. Such future work will build upon the targets identified in our work here, which combine the simultaneous and coupled effects of both texture and viscoelastic fluid properties.

Funding information This work was supported by the National Science Foundation under Grant No. CMMI-1463203. The authors also gratefully acknowledge support from the Procter & Gamble Company.

Publisher's note Springer Nature remains neutral with regard to jurisdictional claims in published maps and institutional affiliations.

References

- Ashmore J, Shen AQ, Kavehpour HP, Stone HA, McKinley GH (2008) Coating flows of non-Newtonian fluids: weakly and strongly elastic limits. *J Eng Math* 60(1):17–41. <https://doi.org/10.1007/s10665-007-9152-8>
- Atalik K, Keunings R (2004) On the occurrence of even harmonics in the shear stress response of viscoelastic fluids in large amplitude oscillatory shear. *J Non-Newtonian Fluid Mech* 122(1):107–116. <https://doi.org/10.1016/j.jnnfm.2003.11.012>
- Batra RL, Mohan V (1978) Roller bearing lubrication with shear thinning lubricants. *Wear* 51(2):213–225. [https://doi.org/10.1016/0043-1648\(78\)90261-2](https://doi.org/10.1016/0043-1648(78)90261-2)
- Bird RB, Armstrong RC, Hassager O (1987) Dynamics of polymeric liquids, vol 1 Fluid Mechanics, 2nd edn. Wiley, New York. ISBN 978-0-471-80245-7
- Corman RE, Rao L, Bharadwaj NA, Allison JT, Ewoldt RH (2016) Setting material function design targets for linear viscoelastic materials and structures. *J Mech Des* 138(5):051402. <https://doi.org/10.1115/1.4032698>
- Criminale WO Jr, Ericksen JL, Filbey GL Jr (1957) Steady shear flow of non-Newtonian fluids. *Arch Ration Mech Anal* 1(1):410–417. <https://doi.org/10.1007/BF00298018>
- Deb K, Pratap A, Agarwal S, Meyarivan T (2002) A fast and elitist multiobjective genetic algorithm: NSGA-II. *IEEE Trans Evol Comput* 6(2):182–197. <https://doi.org/10.1109/4235.996017>
- Deshmukh AP, Allison JT (2016) Multidisciplinary dynamic optimization of horizontal axis wind turbine design. *Struct Multidiscip Optim* 53(1):15–27. <https://doi.org/10.1007/s00158-015-1308-y>
- Deville MO, Fischer PF, Mund EH (2002) High-order methods for incompressible fluid flow. Cambridge University Press, Cambridge. ISBN 978-0-521-45309-7
- Etsion I (2004) Improving tribological performance of mechanical components by laser surface texturing. *Tribol Lett* 17(4):733–737. <https://doi.org/10.1007/s11249-004-8081-1>
- Ewoldt RH (2014) Extremely soft: design with rheologically-complex fluids. *Soft Robot* 1(1):12–20. <https://doi.org/10.1089/soro.2013.1508>
- Fornberg B (2009) A practical guide to pseudospectral methods. Cambridge University Press, Cambridge. ISBN 978-0-511-62635-7. <https://doi.org/10.1017/CBO9780511626357>
- Freund JB, Ewoldt RH (2015) Quantitative rheological model selection: good fits versus credible models using Bayesian inference. *J Rheol* 59(3):667–701. <https://doi.org/10.1122/1.4915299>
- Gropper D, Wang L, Harvey TJ (2016) Hydrodynamic lubrication of textured surfaces: a review of modeling techniques and key findings. *Tribol Int* 94:509–529. <https://doi.org/10.1016/j.triboint.2015.10.009>
- Hamilton DB, Walowit JA, AC M (1966) A theory of lubrication by microirregularities. *J Basic Eng* 88(1):177–185. <https://doi.org/10.1115/1.3645799>
- Heath MT (2002) Scientific computing: an introductory survey, 2nd edn. McGraw-Hill, New York. ISBN 978-0-07-239910-3
- Herber DR, Allison JT (2019) Nested and simultaneous solution strategies for general combined plant and control design problems. *J Mech Des* 141(1):011402. <https://doi.org/10.1115/1.4040705>
- Hirani H, Athre K, Biswas S (2008) Lubricant shear thinning analysis of engine journal bearings. *Tribol Trans* 44(1):125–131. <https://doi.org/10.1080/10402000108982435>
- Huggins ML (1942) The viscosity of dilute solutions of long-chain molecules. IV. Dependence on concentration. *J Am Chem Soc* 64(11):2716–2718. <https://doi.org/10.1021/ja01263a056>
- Johnston MT, King WP, Ewoldt RH (2015) Shear stress characteristics of microtextured surfaces in gap-controlled hydrodynamic lubrication. *Tribol Int* 82:123–132. <https://doi.org/10.1016/j.triboint.2014.10.005>
- Keunings R (2000) A survey of computational rheology. In: Proceedings of the XIIIth international congress on rheology, pp 7–14
- Kopriva DA (2009) Implementing spectral methods for partial differential equations. Springer, Netherlands, ISBN 978-90-481-2260-8. <https://doi.org/10.1007/978-90-481-2261-5>
- Lee YH, Corman RE, Ewoldt RH, Allison JT (2017a) A multiobjective adaptive surrogate modeling-based optimization (MO-ASMO) framework using efficient sampling strategies. In: Proceedings of the ASME 2017 IDETC/CIE conference, vol 2B. 43rd Design Automation Conference, DETC2017-67541, Cleveland, p V02BT03A023. <https://doi.org/10.1115/DETC2017-67541>
- Lee YH, Schuh JK, Ewoldt RH, Allison JT (2017b) Enhancing full-film lubrication performance via arbitrary surface texture design. *J Mech Des* 139(5):053401–1–13. <https://doi.org/10.1115/1.4036133>
- Lin C, Lee YH, Schuh JK, Ewoldt RH, Allison JT (2018) Efficient optimal surface texture design using linearization. In: Schumacher A, Vietor T, Fiebig S, Bletzinger KU, Maute K (eds) Advances in structural and multidisciplinary optimization: Proceedings of the 12th world congress of structural and multidisciplinary optimization (WCSMO12). Springer, Cham, pp 632–647. https://doi.org/10.1007/978-3-319-67988-4_48
- Macosko CW (1994) Rheology: principles, measurements, and applications. Wiley, New York. ISBN 978-0-471-18575-8
- Malak RJ Jr, Paredis CJJ (2010) Using support vector machines to formalize the valid input domain of predictive models in systems design problems. *J Mech Des* 132(10):101001. <https://doi.org/10.1115/1.4002151>

- Nelson AZ, Ewoldt RH (2017) Design of yield-stress fluids: a rheology-to-structure inverse problem. *Soft Matter* 13(41):7578–7594. <https://doi.org/10.1039/C7SM00758B>
- Oldroyd JG (1950) On the formulation of rheological equations of state. *Proc R Soc A: Math Phys Eng Sci* 200(1063):523–541. <https://doi.org/10.1098/rspa.1950.0035>
- Owens RG, Phillips TN (2002) *Computational rheology*. Imperial College Press, London. ISBN 978-1-86094-186-3
- Pettersson U, Jacobson S (2003) Influence of surface texture on boundary lubricated sliding contacts. *Tribol Int* 36(11):857–864. [https://doi.org/10.1016/S0301-679X\(03\)00104-X](https://doi.org/10.1016/S0301-679X(03)00104-X)
- Reynolds O (1886) On the theory of lubrication and its application to Mr. Beauchamp tower's experiments, including an experimental determination of the viscosity of olive oil. *Philos Trans R Soc Lond* 177:157–234. <https://doi.org/10.1098/rspl.1886.0021>
- Schuh JK (2015a) Surface textures and non-Newtonian fluids for decreased friction in full film lubrication. Master's thesis, University of Illinois at Urbana-Champaign. <http://hdl.handle.net/2142/78561>
- Schuh JK, Lee YH, Allison JT, Ewoldt RH (2015b) Surface textures and non-Newtonian fluids for decreasing friction in lubricated sliding contact. In: 2015 fluid power innovation and research conference. Minneapolis, MN
- Schuh JK, Lee YH, Allison JT, Ewoldt RH (2017) Design-driven modeling of surface-textured full-film lubricated sliding: validation and rationale of nonstandard thrust observations. *Tribol Lett* 65(2):35–1–17. <https://doi.org/10.1007/s11249-017-0818-8>
- Schuh JK (2018) Co-design of surface textures and non-Newtonian fluids for decreased friction. PhD thesis, University of Illinois at Urbana-Champaign, <http://hdl.handle.net/2142/100988>
- Schwarz G (1978) Estimating the dimension of a model. *Ann Stat* 6(2):461–464. <https://doi.org/10.1214/aos/1176344136>
- Shan S, Wang GG (2004) An efficient Pareto set identification approach for multiobjective optimization on black-box functions. *J Mech Des* 127(5):866–874. <https://doi.org/10.1115/1.1904639>
- Steponavičė I, Shirazi-Manesh M, Hyndman RJ, Smith-Miles K, Villanova L (2016) On sampling methods for costly multiobjective black-box optimization. In: *Advances in Stochastic and deterministic global optimization*. Springer, Cham. ISBN 978-3-319-29975-4, pp 273–296. https://doi.org/10.1007/978-3-319-29975-4_15
- Suh NP, Mosleh M, Howard PS (1994) Control of friction. *Wear* 175(1-2):151–158. [https://doi.org/10.1016/0043-1648\(94\)90178-3](https://doi.org/10.1016/0043-1648(94)90178-3)
- Tax DM, Duijn RP (1999) Support vector domain description. *Pattern Recogn Lett* 20(11-13):1191–1199. [https://doi.org/10.1016/S0167-8655\(99\)00087-2](https://doi.org/10.1016/S0167-8655(99)00087-2)
- Varenberg M, Halperin G, Etsion I (2002) Different aspects of the role of wear debris in fretting wear. *Wear* 252(11-12):902–910. [https://doi.org/10.1016/S0043-1648\(02\)00044-3](https://doi.org/10.1016/S0043-1648(02)00044-3)
- Wakuda M, Yamauchi Y, Kanzaki S, Yasuda Y (2003) Effect of surface texturing on friction reduction between ceramic and steel materials under lubricated sliding contact. *Wear* 254(3-4):356–363. [https://doi.org/10.1016/S0043-1648\(03\)00004-8](https://doi.org/10.1016/S0043-1648(03)00004-8)
- Wang GG, Shan S (2007) Review of metamodeling techniques in support of engineering design optimization. *J Mech Des* 129(4):370–380. <https://doi.org/10.1115/1.2429697>
- Wilson B, Cappelleri D, Simpson TW, Frecker M (2001) Efficient Pareto frontier exploration using surrogate approximations. *Optim Eng* 2(1):31–50. <https://doi.org/10.1023/A:1011818803494>
- Xiaodi L, Haosheng C, Darong C, Jiadao W (2009) Normal stress effects in journal bearing lubrication with maxwell fluid. In: Luo J, Meng Y, Shao T, Zhao Q (eds) *Advanced tribology*. Springer, Berlin, pp 231–234. https://doi.org/10.1007/978-3-642-03653-8_73
- Yu H, Wang X, Zhou F (2010) Geometric shape effects of surface texture on the generation of hydrodynamic pressure between conformal contacting surfaces. *Tribol Lett* 37(2):123–130. <https://doi.org/10.1007/s11249-009-9497-4>

Affiliations

Yong Hoon Lee¹  · Jonathon K. Schuh² · Randy H. Ewoldt³ · James T. Allison⁴

Jonathon K. Schuh
schuh4@illinois.edu

Randy H. Ewoldt
ewoldt@illinois.edu

James T. Allison
jtalliso@illinois.edu

¹ Mechanical Science and Engineering, University of Illinois at Urbana-Champaign, 1206 W. Green St., #153 MEB, MC-244, Urbana, IL 61801, USA

² Electrical and Computer Engineering, University of Illinois at Urbana-Champaign, 306 N Wright St., #4066 ECEB, Urbana, IL 61801, USA

³ Mechanical Science and Engineering, University of Illinois at Urbana-Champaign, 105 S. Mathews Ave., #4411 MEL, Urbana, IL 61801, USA

⁴ Industrial and Enterprise Systems Engineering, University of Illinois at Urbana-Champaign, 104 S. Mathews Ave., #313 TB, Urbana, IL 61801, USA